

Radial growth of twist-stacked covalent organic framework nanofibers

Received: 21 June 2025

Accepted: 10 November 2025

Published online: 14 December 2025

Check for updates

Xiao-Rui Ren ^{1,4}, Baichuan Kou ^{1,4}, Qing Hao ¹, Francesco Bertocchi², Ying Xu¹, Lu Wang¹, Zhen-Lian Zhao^{1,3}, Ting Chen ¹, Li-Jun Wan ^{1,3} & Dong Wang ^{1,3} ✉

Engineering symmetry breaking is a fertile ground to develop innovative materials with fascinating properties. Herein, we introduce crystallographically incompatible rotation element into two-dimensional polymers and construct twist-stacked covalent organic framework nanofibers (abbreviated as *t*-COFs). These *t*-COFs are derived from polymerization between 2,4,6-triformylphloroglucinol and diamines modulated by monodentate alkylamine. Comprehensive electron microscopy analysis reveals their well-defined fibrous morphology and twist-stacking details. The time-dependent growth process study discloses a new radial growth pattern, which enables *t*-COFs to inherit twist-stacking from hexagonal macrocycle nanotube intermediate. Intriguingly, the twist-stacking mode is found to be intrinsic when using amine modulator, and enantiomeric bias towards one stacking direction can be achieved using chiral amine. Disrupting the inversion symmetry, the consecutive regular rotation of COF layers endows COF nanofibers with structural chirality and large chiroptical response.

Structural modulation is vitally important for manipulating the properties and functions of condensed materials. While traditional crystals are characterized by well-defined lattice structures, breaking symmetry confers great potential to explore new phases of matter. For example, the disruption of three-dimensional translational symmetry brings about the new branch of aperiodic crystals, which involves incommensurate crystals and quasicrystals¹. The twisted and helical arrangements are relevant to reduced symmetries in assembled systems, such as natural biomaterials, supramolecular gels, and liquid crystals, dictating intriguing structural chirality and nonlinear optical properties^{2–4}. Notably, the recent emergence of twisted two-dimensional (2D) materials introduces a new paradigm to engineer symmetry breaking, although twist operation is generally considered incompatible with traditional crystals. By virtue of weak interlayer van der Waals interactions, atomic layers can be stacked with a tailor-made interlayer twist angle. These precise twisted heterostructures,

including bilayer/few-layer superlattices^{5,6} and multilayer nanowires/spirals^{7–9}, have sparked the exploration of exotic physical behaviors. Discovery and on-demand synthesis of new matter with reduced symmetries is actively pursued to develop innovative materials with fascinating electrical and optical properties, and to facilitate cutting-edge applications in nonlinear optics, quantum information science, and biochemistry.

Covalent organic frameworks (COFs) are a distinctive class of organic crystalline materials created by linking molecular building units through covalent bonds¹⁰. Because of their predictable and well-ordered architectures, COFs have emerged as an ideal platform for targeted synthesis and structure–property study^{11–15}. At the molecular level, performance-related functional groups can be readily installed on the backbone^{16,17} or side chains¹⁸ with atomic precision. COFs also possess abundant geometrical structures: polygonal lattices of different topologies can extend in the one-, two-, or three-dimensional

¹CAS Key Laboratory of Molecular Nanostructure and Nanotechnology, CAS Research/Education Center for Excellence in Molecular Sciences, Beijing National Laboratory for Molecular Sciences (BNLMS), Institute of Chemistry, Chinese Academy of Sciences, Beijing, PR China. ²Department of Chemistry, Life Sciences and Environmental Sustainability, University of Parma, Parma, Italy. ³University of the Chinese Academy of Sciences, Beijing, PR China. ⁴These authors contributed equally: Xiao-Rui Ren, Baichuan Kou. ✉e-mail: wangd@iccas.ac.cn

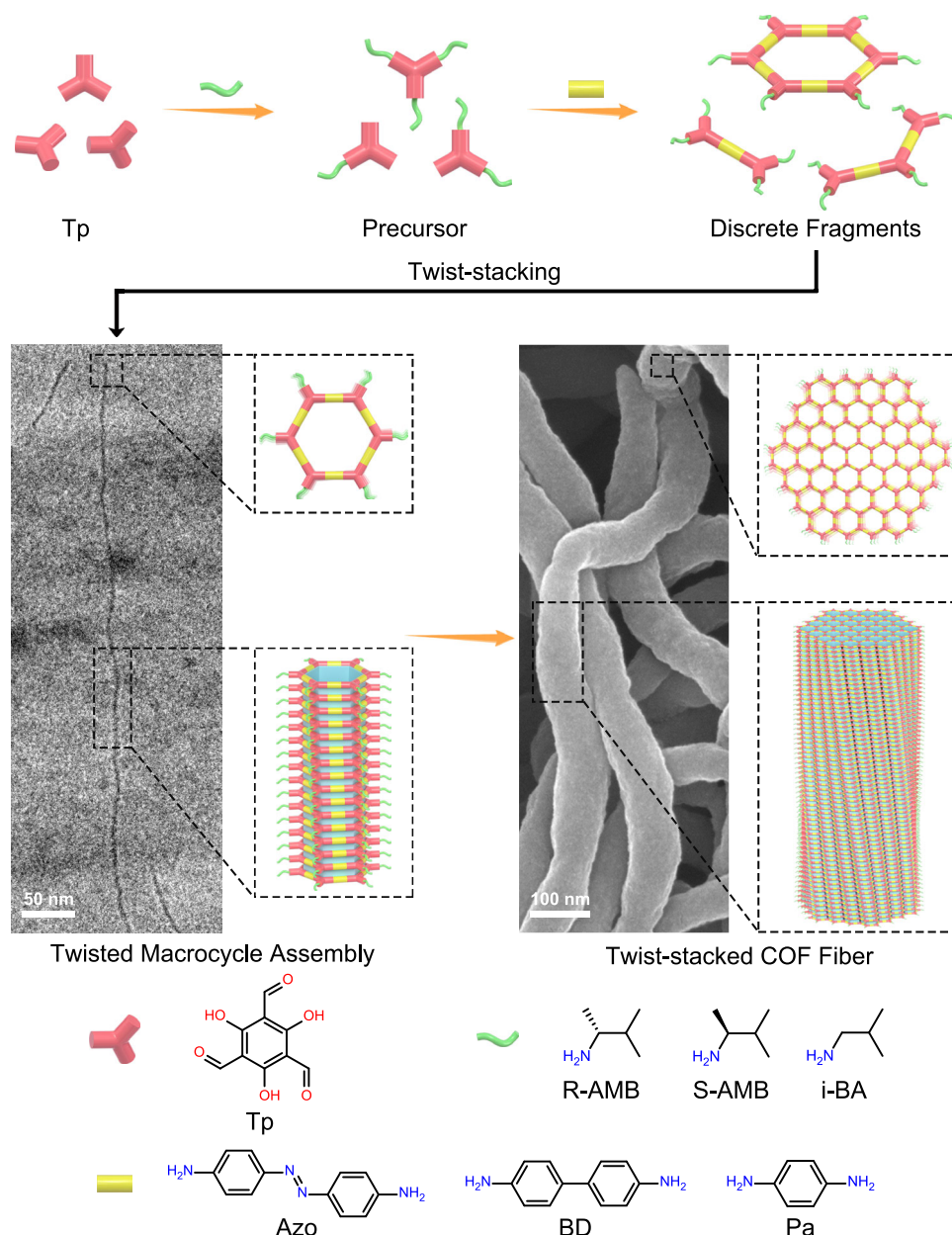


Fig. 1 | Schematic diagram of modulator-assisted synthesis of *t*-COFs. In a general synthetic procedure, the aldehyde linker Tp first reacts with the amine modulator to form the protected precursor. Then the diamine linker is added to the reacting system and undergoes an imine-exchange process with the modulator.

The slow exchange process yields a hexagonal macrocycle intermediate, which is prone to stack into the twisted nanotubes. Further radial growth produces the twist-stacked COF fibers with increasing width.

space^{19,20}. Various stacking²¹ and interpenetration²² manners further enrich the design freedom. On a larger scale, crystal sizes²³ and morphologies²⁴ are of great importance to tailor their physicochemical properties. So far, the above-mentioned perspectives are mostly limited to the realm of periodic structures following basic principles of reticular chemistry. Along with the continuous efforts to pursue COF materials with high crystallinity^{25–37}, introducing aperiodic structural elements to break high symmetry, such as twisted structural motifs^{38–40}, to further unfold novel structures and properties unachievable in traditional crystalline structures, becomes possible but is rarely explored.

Here, we report the general synthesis and chiral control of twist-stacked COFs (*t*-COFs), which are built from entirely achiral monomers. The key step is in-situ formation of hexagonal macrocycle self-assembly at the initial reaction stage, by using

monofunctional alkylamine as a modulator to precisely control over the preferential growth direction (in-plane covalently extending vs. out-of-plane stacking). With twisted macrocycle nanotubes serving as crystal seed, *t*-COF nanofibers with tunable diameters were created through a radial growth process (Fig. 1). Comprehensive electron microscopy analysis was conducted to decipher their twisted architecture: the covalently bonded 2D nanosheets progressively rotate with a fixed small angle along the *c*-axis. The consecutive rotation breaks the inversion and translational symmetry, which is essentially distinct from typical eclipsed, staggered, serrated, or inclined stacking modes in 2D COFs. Notably, twist-stacking results in a highly ordered chiral skeleton that exhibits a large chiroptical response. The highest absolute dissymmetric factor of *t*-COFs is about 0.05 for absorption and 0.04 for luminescence, standing out among organic materials.

Results

Modulator-assisted synthesis of *t*-COFs

Introducing monodentate amine modulator in COF polymerization, like aniline²⁵, has proven to be a powerful method to improve the material crystallinity. Intriguingly, we found the formation of twist-stacking mode in highly crystalline 2D COFs in a modulator-assisted synthetic process. The synthesis and structure characterization of *t*-COFs were first demonstrated on a β -ketoenamine-linked COF, TpAzo (Tp and Azo stand for 2,4,6-triformyl-phloroglucinol and 4,4'-azodianiiline, respectively). Direct solvothermal condensation of Tp and Azo in 1,4-dioxane afforded irregular nanoparticles (Supplementary Fig. 1a). The morphology gradually transitioned to nanofibers upon adding (R)-(-)-2-amino-3-methylbutane (R-AMB) (molar ratio of R-AMB to Tp at 1.5:1 and beyond), as evidenced by scanning electron microscopy (SEM) images (Supplementary Fig. 1b–h). The width of the fibers can be tuned in the range of 30–120 nm, depending on the molar ratio of modulator to monomer. Under the optimized condition, powder X-ray diffraction (PXRD) patterns of the well-defined fibers showed significantly narrowed peaks (full width at half-maximum value of (100) facet was decreased from 0.47° to 0.21°), along with 10-fold intensity enhancement compared to the directly polymerized analog (Supplementary Fig. 2). In addition, Brunauer–Emmett–Teller (BET) surface areas and chemical stability were significantly improved (Supplementary Figs. 3–5). The dramatically boosted crystallinity allows for comprehensively deciphering their crystalline structures via high-resolution transmission electron microscopy (HRTEM).

Identification of twist-stacking mode

COF nanofibers with a diameter of ~85 nm produced via modulation of R-AMB were selected as a representative to study the underlying nanostructures. SEM imaging reveals that micrometer-long COF fibers entangle into dense meshes (Fig. 2a). Figure 2b shows an HRTEM image of the cross-section of COF fibers with overlaid blue hexagons representing the COF backbone. The bright dots in Fig. 2b, corresponding to honeycomb pores, are orderly arranged into a six-fold-symmetric structure. The separation between two centers of bright dots is measured to be (3.23 ± 0.08) nm, consistent with the *ab*-plane cell parameters determined from the PXRD pattern ($a = b = 32.6$ Å). According to the hexagon-overlaid HRTEM image, we depicted the schematic drawing of the cross-section, which manifests the spacings of (100) and (110) planes, as shown in Fig. 2c.

If 2D COF nanosheets are stacked in an eclipsed AA manner, long continuous pore channels should be observed along the *c*-axis²⁷. To our surprise, only short intermittent fringes are visible (Fig. 2d). There are two types of lattice fringes indicated by green and orange arrows, respectively. The fringes marked by the green arrow exhibit a spacing of 2.80 nm, and the orange fringes with a spacing of 1.63 nm consistently appear in the middle between two sets of green fringes (Fig. 2e). Considering the spacing and spatial position, the green and orange fringes are assigned to (100) and (110) planes, respectively. The regular intermittence periods plus well-ordered arrangement in *ab*-plane represent the signature characters of axial twisted channels^{38,41,42}.

To verify the twisted channel structure, an individual COF fiber with *c*-axis parallel to the rotation axis of sample holder was incrementally tilted within the range from -30° to +30° (Fig. 2f and Supplementary Fig. 6). We observed that the position of fringes is continuously moving during rotation and the position after tilting to -30° is identical to that after tilting to +30°. These results suggest the presence of chiral channels of six-fold rotational symmetry. The chiral channels are the result of twisted stacking, that is, COF nanosheets in these fibers progressively rotate around the central axis with a fixed angle. The orthographic projection images based on such a structural model match well with the experimental results (Supplementary Fig. 6d), further confirming the generation of the twist-stacking mode. According to the transmission electron microscopy (TEM) images, the

chiral pitch, six times the distance between two sets of (100) fringes, is measured to be 700–800 nm. The corresponding twisted angle is 0.16–0.18° per layer.

Notably, the moving direction of fringes in Fig. 2f is relevant to the twisted direction, i.e., left-handed *t*-COFs exhibit upward movement while right-handed samples show a downward trend. The twisted direction can be further inferred by the curvature direction of fringes when the fiber is not precisely perpendicular to the electron beam (Supplementary Fig. 7). Taking a horizontal fiber with *c*-axis normal to the rotation axis of sample holder as an example, if the fringes curve downwards as the TEM holder is tilted anticlockwise, this fiber is determined to be left-handed (Supplementary Fig. 8). On the contrary, right-handed fibers exhibit upward-curving (100) fringes when they are tilted to the same direction. Six horizontal fibers modulated by R-AMB (*t*-TpAzo-R-AMB) were measured, and five out of them were left-handed (Supplementary Fig. 9). The introduction of (S)-(+)-2-amino-3-methylbutane (S-AMB), the enantiomer of R-AMB, also yielded twisted COF fibers (*t*-TpAzo-S-AMB), and the majority were right-handed (Supplementary Fig. 10).

Generality of modulator-assisted synthesis and chiroptical properties of *t*-COFs

We next demonstrated the generality of this synthetic strategy for another two diamines, benzidine (BD) and *p*-phenylenediamine (Pa). Twist-stacked COF nanofibers (*t*-TpBD-R/S-AMB and *t*-TpPa-R/S-AMB) were created under similar solvothermal conditions, as proven by regularly spaced fringes in TEM images (Supplementary Figs. 11 and 16). Based on the intermittence period of (100) fringes, the chiral pitches of *t*-TpBD-R/S-AMB and *t*-TpPa-R/S-AMB are calculated to be ~600 nm and ~400 nm, respectively. Accordingly, the twisted angles are -0.21° and -0.30°, respectively. These chiral COF fibers exhibited superior crystallinity relative to their analogs prepared in the absence of a modulator (Supplementary Figs. 12 and 17). There was no apparent difference in the PXRD pattern shape and peak positions between twisted fiber and achiral COFs, which can be rationalized by the little twisted angle. Also, these *t*-COFs exhibit high BET surface areas along with excellent chemical and thermal stability (Supplementary Figs. 13–15 and 18–20).

The stacking geometry is of great importance to layered 2D polymeric materials. It not only defines the pore shape and size but also has a profound impact on multiple properties, such as guest inclusion⁴³, catalytic capability²¹, charge transport⁴⁴, and fluorescence⁴⁵. Most of the 2D COF nanosheets are stacked in an eclipsed, staggered, serrated, or inclined manner. Twist-stacking is distinguished from these modes by the resulting structural chirality. Hence, we studied chiroptical properties of prepared *t*-COFs.

As depicted in Fig. 3a, *t*-TpAzo-R/S-AMB exhibits strong electronic circular dichroism (ECD) signals in the range of 500–600 nm, which are nearly mirror images of each other. This indicates that the products modulated by R- and S-AMB are a pair of enantiomers. Based on the TEM analysis, the correlation between the twisted direction of *t*-COF fibers and ECD signals can be established. The maximum absolute dissymmetric factor ($|g_{\text{abs}}|$) value is about 0.05 (Supplementary Fig. 21a), which is much larger than most organic small-molecule or supramolecular systems and the reported pure COF materials (Supplementary Table 1)^{3,46}. The strong chiroptical response originates from chiral aggregation of achiral COF building blocks. Chiral impurity contributes little since the non-aromatic modulator has no absorption in the visible range. Light scattering is a key element that should be taken into consideration when it comes to nanoscale, submicrometer-scale, or micrometer-scale chirality⁴⁷. We observed that the scattering effect can be ignored for *t*-COFs with a width smaller than 100 nm (Supplementary Fig. 22). Additionally, the chiroptical properties at the excited states were studied by circularly polarized luminescence (CPL) spectra. Both *t*-TpAzo-R-AMB and *t*-TpAzo-S-AMB display intense CPL

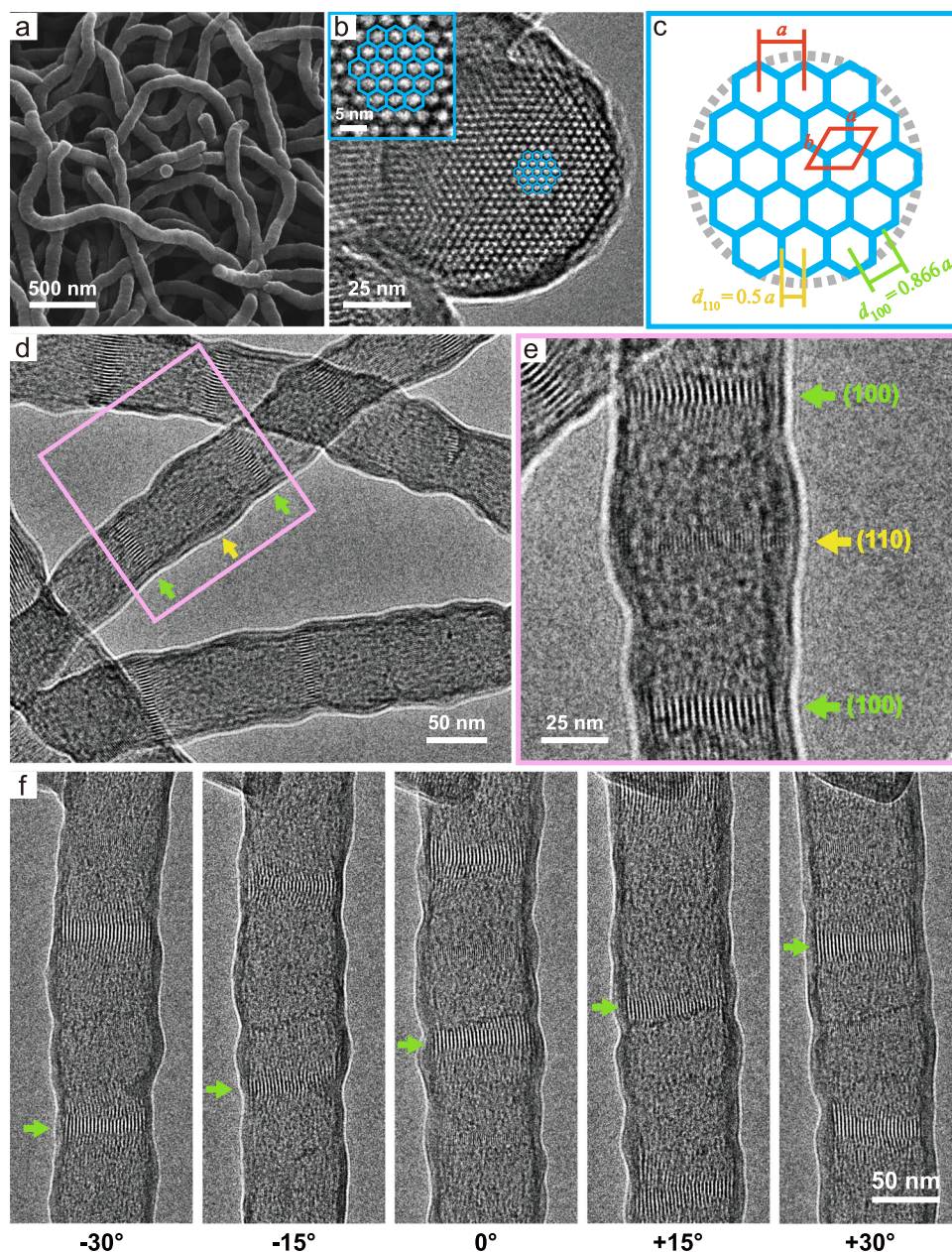


Fig. 2 | Electron microscopy characterization of *t*-COF nanofibers prepared in the presence of R-AMB. **a** SEM image of the dense COF fibers of ~85 nm diameter and micrometer-scale lengths. **b** HRTEM image of the cross-section where bright dots correspond to the COF pores. Inset: magnified view of the hexagon-overlaid area. **c** A schematic drawing of the cross-section, which manifests an *ab*-plane cell together with the spacings of (100) and (110) planes. **d** A low-magnification TEM

image of the COF fibers. The short and intermittent lattice fringes were observed along the axial direction. **e** The magnified view of the selected square area in **(d)**. The green and orange arrows indicate (100) and (110) fringes, respectively. **f** The evolution of TEM images when a vertical fiber is tilted around its central *c*-axis, ranging from -30° to $+30^\circ$. The position of lattice fringes moves during rotation, and the position after tilting to -30° is identical to that after tilting to $+30^\circ$.

emission at about 620 nm with positive and negative signals, respectively (Fig. 3b). The absolute dissymmetric factor ($|g_{lum}|$) value is as high as 0.04 (Supplementary Fig. 21b), also standing out among organic materials (Supplementary Table 1)⁴⁸.

Likewise, *t*-TpBD and *t*-TpPa exhibited obvious ECD and CPL signals (Fig. 3c–f and Supplementary Figs. 23 and 24). The ECD spectra of these *t*-COFs showed analogous profiles with different absorption maxima. This suggests chiral spectroscopic signatures correlate with the long-range twisted order (shape and strength), twisted direction dependent on modulator (positive or negative sign), and chromophores in the COF skeleton (maximum position and strength). To date, chiral COFs highly rely on intrinsic^{49,50} or induced^{51–53} chiral centers, with a few examples demonstrating the chirality manifestation at the

unit cell level to chiral topology^{54–56} and at the macroscopic level to helical morphology^{57–61}. The twist stacking is an independent chiral element at the aggregation level, which, in most cases, naturally breaks the translational symmetry (with few exceptions in chiral space groups), and makes *t*-COFs an ordered but aperiodic material. We emphasize that twist stacking and the *t*-COFs could form from achiral monomers (*vide infra*). The general synthesis of *t*-COFs adds to the diversity of chiral COFs and opens a new perspective on precise control of crystallinity, chirality, and functionality.

Spontaneous self-resolution process

Herein, a question arises whether a chiral modulator is necessary for the generation of the twist-stacking mode. We selected TpAzo as a

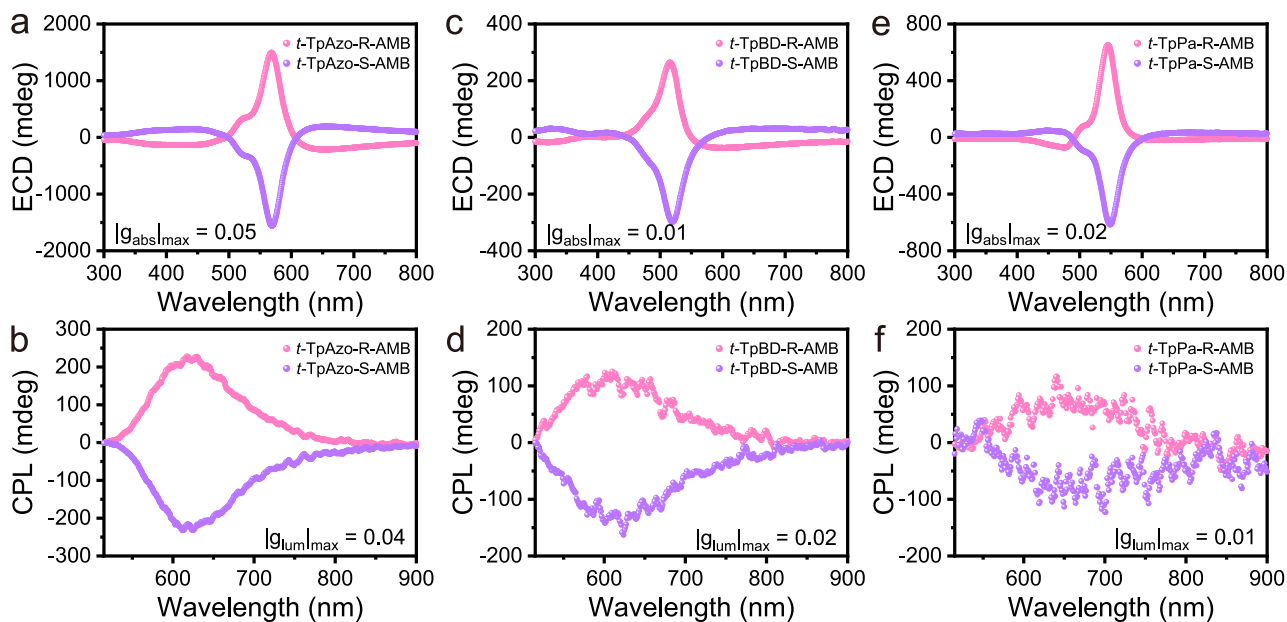


Fig. 3 | Chiroptical properties of *t*-COFs. ECD spectra of *t*-TpAzo-R/S-AMB (a), *t*-TpBD-R/S-AMB (c), *t*-TpPa-R/S-AMB (e) dispersed in EtOH. CPL spectra of *t*-TpAzo-R/S-AMB (b), *t*-TpBD-R/S-AMB (d), *t*-TpPa-R/S-AMB (f) dispersed in EtOH (excitation at 400 nm).

model system and conducted the reaction using isobutylamine (i-BA) as an achiral modulator. Twisted fiber (*t*-TpAzo-i-BA) of high quality was still generated (Supplementary Fig. 25). However, both left and right-handed fibers were observed without an enantiomeric excess (Supplementary Figs. 26–28). Intriguingly, we observed the coexistence of two chiral directions in one twisted fiber, as shown in Fig. 4. The orange frame presents the transition from left-handedness to right-handedness. As expected, *t*-TpAzo-i-BA exhibits no ECD signal (Supplementary Fig. 29), confirming that a bulk racemate of two chiral directions formed.

The above analyses regarding HRTEM and ECD characterization indicate that the formation of twist-stacking is intrinsic to Tp COFs in the presence of an amine modulator. A spontaneous self-resolution process, where achiral components arrange in a chiral form to generate separate enantiomer aggregates^{62,63}, occurred during the polymerization (Supplementary Fig. 30). Both achiral and chiral modulators can induce self-sorting, which produces *t*-COF fibers with two twist directions. The former yields left- and right-handed pieces in an equal number, whereas the latter can bias the synthesis in favor of one mirror image to achieve chiral control.

Radial growth pattern of *t*-COFs

To gain insight into the origin of twist-stacking, we probed the growth process of *t*-TpAzo-R-AMB by carrying out ex-situ characterization of products collected at different reaction time intervals by TEM, atomic force microscopy (AFM), absorption, as well as ECD spectroscopy. TEM and AFM imaging revealed that nanotubes with a diameter of (4.0 ± 0.7) nm and length of submicron gradually form at the initial stage (1 h, depicted in Fig. 5a–c). These relatively short nanotubes are ascribed to the self-assembly of hexagonal molecular macrocycles containing 12 β -ketoenamine linkages because of the well-matched size. In the case of 3 h, fine nanofibers of (9.7 ± 1.2) nm diameter are observed, accompanied by short nanotubes of 4.0 nm diameter (Fig. 5e). As the reaction proceeds to 5 h, 10 h, and 15 h, the widths of fine fibers increase to (15.7 ± 1.8) nm, (28.5 ± 3.5) nm, and (35.6 ± 3.9) nm, respectively (Fig. 5f, g and Supplementary Fig. 31a). Meanwhile, these fibers show an elongation up to several micrometers. Further extension of the reaction time to 72 h leads to a progressive increase in width, which finally reaches (85.6 ± 9.1) nm (Fig. 5h, i and

Supplementary Fig. 31b). Furthermore, the HRTEM images of fine fibers with width of ~ 35 nm (the fragile nature of organic nanofiber precludes HRTEM imaging of thinner fibers) showed clear separated (100) fringes as well (Supplementary Fig. 32). The chiral pitch is estimated to be 600–800 nm, indicating that the degree of twist exhibits inconspicuous change during growth process.

Along with the increase in width of samples, the absorption band undergoes a bathochromic shift (Fig. 5j). The strongest band varies from 460 nm to 500 nm in the first 10 h, and then the absorption at 550 nm slowly climbs. On the other hand, ECD spectra show two intense Cotton effects with two crossovers. When *t*-COF fiber gets thicker, the signal at longer wavelength rises more rapidly than the shorter-wavelength one (Fig. 5k). It can also be observed that a positive correlation exists between maximum g_{abs} and the diameter of *t*-COF nanofiber (Fig. 5l). As depicted in Fig. 5d, the area of the conjugated system is increasing, and the misalignment between adjacent layers becomes larger with the growth of *t*-COF fibers. These variations may greatly affect the coupling between chromophores and the electronic transition process⁶⁴, accounting for the dramatically boosted ECD signals for thick *t*-COF nanofibers.

Based on the above experimental results, a new radial growth mechanism, as illustrated in Fig. 1, is proposed. In principle, crystallization of 2D COFs includes in-plane growth (covalent bond formation and breakage) and out-of-plane stacking (mainly driven by π - π interactions) process. For typical bulk synthesis, 2D COFs are considered to simultaneously extend in two directions⁶⁵ since no clear anisotropic evolution has been observed. In stark contrast, we achieved the separation of two growing processes in modulator-assisted synthesis of *t*-COFs. Compared to out-of-plane stacking, the in-plane growth rate is significantly limited by slow amine exchange based on a less reversible β -ketoenamine linkage. This makes macrocycles a stable intermediate with a long lifetime enough for the formation of self-assembled nanotubes, which were observed at the initial reaction stage. The later stage witnessed a well-defined transition from nanotubes to fine fibers to thick fibers, unequivocally indicative of a dominant radial growth pattern. Due to π - π repulsion and/or steric hindrance, the modulator-terminated macrocycles prefer to assemble into a twisted form rather than an eclipsed stack, as evidenced by the emergence of a new ECD signal at longer wavelengths compared with

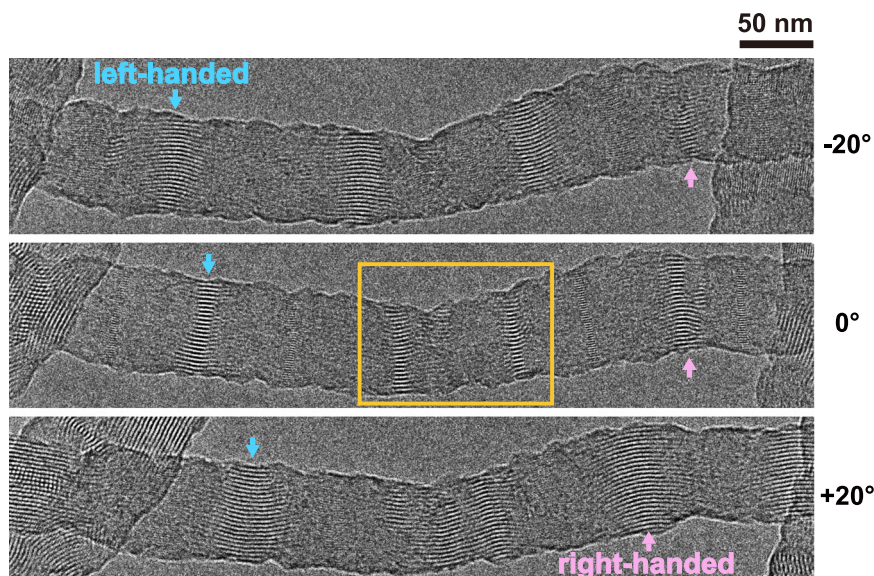


Fig. 4 | Co-existence of two chiral directions in one twisted fiber. The evolution of HRTEM images of *t*-TpAzo-i-BA when a horizontal fiber is tilted by a degree ranging from -20° to $+20^\circ$. The orange frame presents the transition from left-handedness to right-handedness.

the precursor (Supplementary Fig. 33). In fact, the formation of non-eclipse stacked imine-linked macrocycles⁶⁶ and Tp-based liquid crystals⁶⁷ has been reported. With twisted macrocycle assembly serving as a crystal seed, subsequent radial growth enables the generation of *t*-COFs with a remaining degree of twist. These findings broaden our understanding of molecular aggregation behavior under combined covalent/non-covalent interactions, paving the way for controlled synthesis of complex systems.

Discussion

In summary, we have demonstrated the construction of unexpected *t*-COFs via a facile modulation approach. These *t*-COFs follow a radial growth pattern and show readily tunable structural parameters. The effects of chemical composition, fiber diameter, and twisted direction on their chiroptical properties were studied. *t*-COFs provide a novel molecular aggregate model for fundamental studies. The disk-shaped aromatic knots in *t*-COFs arrange into a nonperiodic twisted bundle, unlike a periodic 2D array in columnar phases of discotic liquid crystals⁶⁸. The discrete helical channels of *t*-COFs resemble the filaments in biological or synthetic twisted yarns, such as fibrin fibers⁶⁹ and coiled polymer muscles⁷⁰. Moreover, the growth process results and structural analysis of *t*-COFs indicate that the twist-stacking mode in *t*-COFs is distinctly different from the Eshelby twist observed in some inorganic materials^{7,8}, which is based on the progression of the spiral defects. It is anticipated that this synthetic strategy for *t*-COFs can be applied to a rich library of building units, not confined to the Tp-based category with hcb topology. There is also plenty of room to fabricate fascinating hierarchical or hybrid systems using *t*-COFs as a structural motif. By virtue of a unique aperiodic-order feature and great engineering potential, *t*-COFs would advance the rational synthesis and functionalization of novel architectures, as well as their applications in asymmetric synthesis, nonlinear optics, multiferroics, spintronics, and so on.

Methods

Materials

General solvents and reagents were obtained from Acros Organics and Concord Technology (Tianjin) Co., Ltd. The monomer of 2,4,6-triformylphloroglucinol (Tp, purity $\geq 98\%$), 4,4'-azodianiline (Azo, purity $\geq 97\%$) and benzidine (BD, purity $\geq 98\%$) were purchased from Jilin Chinese Academy of Sciences - Yanshen Technology Co., Ltd.

p-Phenylenediamine (Pa, purity $\geq 98\%$) and acetic acid (CH_3COOH , purity $\geq 99.5\%$) were purchased from TCI chemicals. The modulator of (R)-(-)-2-amino-3-methylbutane (R-AMB, purity $\geq 98\%$, ee 97%), (S)-(+)-2-amino-3-methylbutane (S-AMB, purity $\geq 98\%$, ee 97%), and isobutylamine (i-BA, purity $\geq 99.5\%$) were purchased from Shanghai Aladdin Biochemical Technology Co., Ltd. All chemicals were used without further purification.

Typical solvothermal synthesis of TpAzo

Tp (15.8 mg, 0.08 mmol) and Azo (23.9 mg, 0.12 mmol) were weighed into a 10 mL Schlenk tube. Afterwards, 1,4-dioxane (1.5 mL) was added and the mixture was sonicated for 10 min. After the addition of 0.3 mL of 6 M aqueous acetic acid, the tube was degassed by the three freeze–pump–thaw cycles. Upon warming to room temperature, the Schlenk tube was heated at 120°C for 3 days. The formed precipitate was collected by filtration, washed with tetrahydrofuran (THF), and further activated by Soxhlet extraction using THF for 24 h. Finally, the solid was collected and dried at 80°C for 12 h to give TpAzo as a red powder (45.9 mg, 87% yield).

Modulator-assisted synthesis of *t*-TpAzo-R/S-AMB

A 10 mL Schlenk tube was charged with Tp (15.8 mg, 0.08 mmol), R-AMB/S-AMB (8.75–26.25 μL , 1–3 equiv.), and 1,4-dioxane (1.5 mL). The mixture was sonicated for 10 min followed by the addition of Azo (23.9 mg, 0.12 mmol) and 6 M aqueous acetic acid (0.3 mL). After sonicated for more 10 min, the tube was degassed by the three freeze–pump–thaw cycles. Upon warming to room temperature, the Schlenk tube was heated at 120°C for 3 days. The formed precipitate was collected by filtration, washed with THF, and further activated by Soxhlet extraction using THF for 24 h. Finally, the solid was collected and dried at 80°C for 12 h to give *t*-TpAzo-R/S-AMB as a red powder (see COF yield in Supplementary Fig. 2d).

TEM characterization

The evolution of morphology in the growing process was monitored by TEM using JEOL JEM-2100F operating at 200 kV. Samples obtained in the reaction interval of 1–5 h were diluted with EtOH and then directly dropped onto ultra-thin holey carbon film supported copper grids (300 mesh). Samples obtained after 5 h were slightly washed with EtOH, followed by sonication in EtOH suspension for characterization. For the statistical analysis of nanofibers' diameter,

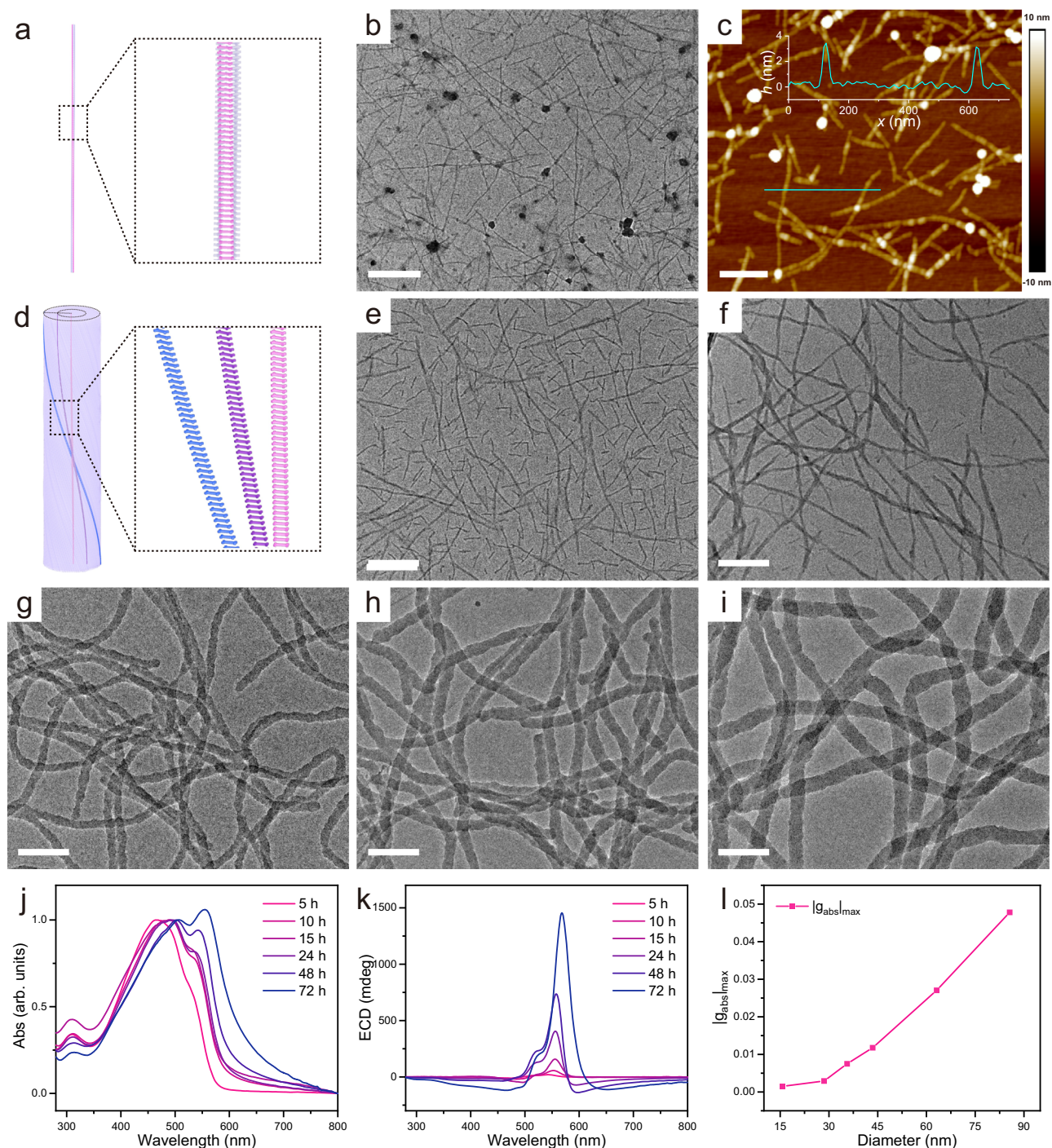


Fig. 5 | Monitoring the growth process of *t*-TpAzo-R-AMB. **a** Schematic illustration, **b** TEM image, and **c** AFM height image of the product obtained at 1 h. **d** Schematic illustration of the product obtained at 72 h. TEM images of samples obtained at reaction time intervals of 3 h (**e**), 5 h (**f**), 15 h (**g**), 24 h (**h**), and 48 h (**i**).

j Absorption and **k** ECD spectra of products prepared at different time intervals. **l** The correlation chart between the diameter of nanofibers and $|g_{\text{abs}}|_{\text{max}}$. The scale bars are 200 nm in (**b**, **e**–**i**) and 300 nm in (**c**).

five parallel experiments were performed at each monitored time point. Among them, three samples with relatively consistent diameter distributions were selected, and 30–40 nanofibers from each sample were measured. In total, 100 nanofibers were analyzed at each time point to determine the average diameter and the corresponding error range.

The nanostructure of *t*-COFs was characterized by cryo transmission electron microscopy using ThermoFisher Scientific Themis 300 at a working voltage of 300 kV. The micrographs were captured with a Falcon III direct electron detector (ThermoFisher Scientific) at

77 K using a low-dose technique with the dose rate of ~ 5 electrons per \AA^2 per second.

Measurement of chiroptical properties of *t*-COFs

The ECD spectra and UV–vis absorption spectra were simultaneously collected on a JASCO J-1700 CD spectrometer. EtOH dispersions of samples were loaded in a quartz cuvette of 2 mm to record the ECD curves at a scanning rate of 500 nm min^{-1} in the range of 200–800 nm. The g_{abs} spectra were directly transferred from ECD spectra using the Spectra Manager software of JASCO. The CPL spectra were collected

on a JASCO CPL-300 spectrophotometer. EtOH dispersions of samples were loaded in a quartz cuvette of 2 mm to record the CPL curves at a scanning rate of 100 nm min⁻¹ in the range of 500–900 nm. The slits for both the excitation and emission sides were 3000 μm, and the excitation wavelength for all the samples was 400 nm. The *g*_{lum} spectra were directly transferred from CPL spectra using the Spectra Manager software of JASCO.

General characterization

PXRD patterns were collected on a PANalytical Empyrean Diffractometer using Cu K α X-ray radiation ($\lambda = 1.5406 \text{ \AA}$) with 40 kV voltage and 40 mA current. ¹³C cross polarization magic angle spinning nuclear magnetic resonance (¹³C CP/MAS NMR) spectra were recorded on a Bruker AVANCE III 600 NMR spectrometer using a 4-mm double-resonance MAS probe under a spinning frequency of 12 kHz. Fourier transform infrared spectra were obtained from a Bruker VERTEX 70v spectrometer using KBr pellets. N₂ sorption isotherms were measured at 77 K using an Autosorb-IQ instrument after samples were degassed at 100 °C for 8 h under vacuum. Pore size distributions of samples were determined by the quenched solid density functional theory model. The thermogravimetric analysis (TGA) was conducted with Hitachi STA7200RV over the temperature range from 25 °C to 800 °C under N₂ atmosphere at a heating rate of 10 °C min⁻¹. SEM images were taken on a Hitachi Regulus 8100 field-emission scanning electron microscope at an accelerating voltage of 10 kV. AFM height images were collected using a Bruker Multimode 8 AFM in tapping mode. The sample obtained at 1 h was diluted with EtOH and then directly dropped onto a silicon substrate for AFM characterization.

Data availability

The data that support the findings of this study are available within the article and Supplementary Information files. All data are available from the corresponding author upon request. Source data are provided with this paper.

References

- Janssen, T., Chapuis, G. & de Boissieu, M. *Aperiodic Crystals* (Oxford University Press, 2007).
- Webber, M. J., Appel, E. A., Meijer, E. W. & Langer, R. Supramolecular biomaterials. *Nat. Mater.* **15**, 13–26 (2016).
- Liu, M., Zhang, L. & Wang, T. Supramolecular chirality in self-assembled systems. *Chem. Rev.* **115**, 7304–7397 (2015).
- Miyajima, D. et al. Ferroelectric columnar liquid crystal featuring confined polar groups within core-shell architecture. *Science* **336**, 209–213 (2012).
- Cao, Y. et al. Correlated insulator behaviour at half-filling in magic-angle graphene superlattices. *Nature* **556**, 80–84 (2018).
- Yuan, L. et al. Twist-angle-dependent interlayer exciton diffusion in WS₂-WSe₂ heterobilayers. *Nat. Mater.* **19**, 617–623 (2020).
- Sutter, P., Wimer, S. & Sutter, E. Chiral twisted van der Waals nanowires. *Nature* **570**, 354–357 (2019).
- Liu, Y. et al. Helical van der Waals crystals with discretized Eshelby twist. *Nature* **570**, 358–362 (2019).
- Zhao, Y. et al. Supertwisted spirals of layered materials enabled by growth on non-Euclidean surfaces. *Science* **370**, 442–445 (2020).
- Côté, A. P. et al. Porous, crystalline, covalent organic frameworks. *Science* **310**, 1166–1170 (2005).
- Lin, S. et al. Covalent organic frameworks comprising cobalt porphyrins for catalytic CO₂ reduction in water. *Science* **349**, 1208–1213 (2015).
- Vyas, V. S. et al. Exploiting noncovalent interactions in an imine-based covalent organic framework for quercetin delivery. *Adv. Mater.* **28**, 8749–8754 (2016).
- Jin, E. et al. Two-dimensional sp² carbon-conjugated covalent organic frameworks. *Science* **357**, 673–676 (2017).
- Zhang, Q. et al. Covalent organic framework-based porous ionomers for high-performance fuel cells. *Science* **378**, 181–186 (2022).
- Yuan, Y. et al. Selective scandium ion capture through coordination templating in a covalent organic framework. *Nat. Chem.* **15**, 1599–1606 (2023).
- Wang, X. et al. Sulfone-containing covalent organic frameworks for photocatalytic hydrogen evolution from water. *Nat. Chem.* **10**, 1180–1189 (2018).
- Wang, M. et al. Exceptionally high charge mobility in phthalocyanine-based poly(benzimidazobenzophenanthroline)-ladder-type two-dimensional conjugated polymers. *Nat. Mater.* **22**, 880–887 (2023).
- Xu, H., Gao, J. & Jiang, D. Stable, crystalline, porous, covalent organic frameworks as a platform for chiral organocatalysts. *Nat. Chem.* **7**, 905–912 (2015).
- Jin, Y., Hu, Y. & Zhang, W. Tessellated multiporous two-dimensional covalent organic frameworks. *Nat. Rev. Chem.* **1**, 0056 (2017).
- Gropp, C., Ma, T., Hanikel, N. & Yaghi, O. M. Design of higher valency in covalent organic frameworks. *Science* **370**, eabd6406 (2020).
- Wu, X., Han, X., Liu, Y., Liu, Y. & Cui, Y. Control interlayer stacking and chemical stability of two-dimensional covalent organic frameworks via steric tuning. *J. Am. Chem. Soc.* **140**, 16124–16133 (2018).
- Ma, T. et al. Observation of interpenetration isomerism in covalent organic frameworks. *J. Am. Chem. Soc.* **140**, 6763–6766 (2018).
- Ma, T. et al. Diverse crystal size effects in covalent organic frameworks. *Nat. Commun.* **11**, 6128 (2020).
- Sasmal, H. S., Kumar Mahato, A., Majumder, P. & Banerjee, R. Landscaping covalent organic framework nanomorphologies. *J. Am. Chem. Soc.* **144**, 11482–11498 (2022).
- Ma, T. et al. Single-crystal x-ray diffraction structures of covalent organic frameworks. *Science* **361**, 48–52 (2018).
- Evans, A. M. et al. Seeded growth of single-crystal two-dimensional covalent organic frameworks. *Science* **361**, 52–57 (2018).
- Peng, L. et al. Ultra-fast single-crystal polymerization of large-sized covalent organic frameworks. *Nat. Commun.* **12**, 5077 (2021).
- Zhang, W. et al. Reconstructed covalent organic frameworks. *Nature* **604**, 72–79 (2022).
- Kang, C. et al. Growing single crystals of two-dimensional covalent organic frameworks enabled by intermediate tracing study. *Nat. Commun.* **13**, 1370 (2022).
- Natraj, A. et al. Single-crystalline imine-linked two-dimensional covalent organic frameworks separate benzene and cyclohexane efficiently. *J. Am. Chem. Soc.* **144**, 19813–19824 (2022).
- Zhou, Z. et al. Growth of single-crystal imine-linked covalent organic frameworks using amphiphilic amino-acid derivatives in water. *Nat. Chem.* **15**, 841–847 (2023).
- Wang, S. et al. Single-crystal 2D covalent organic frameworks for plant biotechnology. *J. Am. Chem. Soc.* **145**, 12155–12163 (2023).
- Yu, B. et al. Linkage conversions in single-crystalline covalent organic frameworks. *Nat. Chem.* **16**, 114–121 (2024).
- Han, J. et al. Fast growth of single-crystal covalent organic frameworks for laboratory X-ray diffraction. *Science* **383**, 1014–1019 (2024).
- Yi, L., Gao, Y., Luo, S., Wang, T. & Deng, H. Structure evolution of 2D covalent organic frameworks unveiled by single-crystal X-ray diffraction. *J. Am. Chem. Soc.* **146**, 19643–19648 (2024).
- Liu, S. et al. Single-crystal dynamic covalent organic frameworks for adaptive guest alignments. *J. Am. Chem. Soc.* **146**, 34053–34063 (2024).
- Zhang, J. et al. Morphological tuning of covalent organic framework single crystals. *J. Am. Chem. Soc.* **146**, 35090–35097 (2024).
- Zhang, Y.-J. et al. Observation of chiral channels in helical covalent organic frameworks. *J. Am. Chem. Soc.* **146**, 11450–11456 (2024).

39. Sun, J., Peng, L., Liu, Y. & Wei, D. Highly crystalline helical covalent organic frameworks. *Chem. Mater.* **36**, 3666–3672 (2024).
40. Zhan, G. et al. Moiré two-dimensional covalent organic framework superlattices. *Nat. Chem.* **17**, 518–524 (2025).
41. Che, S. et al. Synthesis and characterization of chiral mesoporous silica. *Nature* **429**, 281–284 (2004).
42. Ohsuna, T., Liu, Z., Che, S. & Terasaki, O. Characterization of chiral mesoporous materials by transmission electron microscopy. *Small* **1**, 233–237 (2005).
43. Sick, T. et al. Switching on and off interlayer correlations and porosity in 2D covalent organic frameworks. *J. Am. Chem. Soc.* **141**, 12570–12581 (2019).
44. Cai, S. et al. Reversible interlayer sliding and conductivity changes in adaptive tetrathiafulvalene-based covalent organic frameworks. *ACS Appl. Mater. Interfaces* **12**, 19054–19061 (2020).
45. Albacete, P. et al. Layer-stacking-driven fluorescence in a two-dimensional imine-linked covalent organic framework. *J. Am. Chem. Soc.* **140**, 12922–12929 (2018).
46. Tanaka, H., Inoue, Y. & Mori, T. Circularly polarized luminescence and circular dichroisms in small organic molecules: correlation between excitation and emission dissymmetry factors. *ChemPhotoChem* **2**, 386–402 (2018).
47. Jiang, S. & Kotov, N. A. Circular polarized light emission in chiral inorganic nanomaterials. *Adv. Mater.* **35**, 2108431 (2023).
48. Gong, Z.-L. et al. Frontiers in circularly polarized luminescence: molecular design, self-assembly, nanomaterials, and applications. *Sci. China Chem.* **64**, 2060–2104 (2021).
49. Wang, X. et al. Homochiral 2D porous covalent organic frameworks for heterogeneous asymmetric catalysis. *J. Am. Chem. Soc.* **138**, 12332–12335 (2016).
50. Monroy, J.dR. et al. Homochiral versus racemic 2D covalent organic frameworks. *J. Am. Chem. Soc.* **147**, 17750–17763 (2025).
51. Han, X. et al. Chiral induction in covalent organic frameworks. *Nat. Commun.* **9**, 1294 (2018).
52. Chen, H., Gu, Z.-G. & Zhang, J. Chiral-induced ultrathin covalent organic frameworks nanosheets with tunable circularly polarized luminescence. *J. Am. Chem. Soc.* **144**, 7245–7252 (2022).
53. Weng, W. & Guo, J. The effect of enantioselective chiral covalent organic frameworks and cysteine sacrificial donors on photocatalytic hydrogen evolution. *Nat. Commun.* **13**, 5768 (2022).
54. Hu, Y. et al. Single crystals of mechanically entwined helical covalent polymers. *Nat. Chem.* **13**, 660–665 (2021).
55. Kang, X. et al. Three-dimensional homochiral covalent organic frameworks with intrinsic chiral qzd topology. *J. Am. Chem. Soc.* **146**, 8407–8416 (2024).
56. Zhou, Z. et al. Conformational chirality of single-crystal covalent organic frameworks. *J. Am. Chem. Soc.* **146**, 34064–34069 (2024).
57. Tang, X. et al. Self-assembly of helical nanofibrous chiral covalent organic frameworks. *Angew. Chem. Int. Ed.* **62**, e202216310 (2022).
58. Zha, X. et al. Sculpting mesoscopic helical chirality into covalent organic framework nanotubes from entirely achiral building blocks. *Angew. Chem. Int. Ed.* **63**, e202316385 (2024).
59. Hou, B. et al. Homochiral covalent organic frameworks with superhelical nanostructures enable efficient chirality-induced spin selectivity. *Angew. Chem. Int. Ed.* **63**, e202412380 (2024).
60. Li, S. et al. A facile micelle-assisted self-assembly method to covalent organic framework helical nanoarchitectures. *J. Am. Chem. Soc.* **147**, 11632–11638 (2025).
61. Huang, M. et al. Aqueous synthesis of three-dimensional helical covalent organic frameworks with hierarchical chirality. *Polymer* **318**, 127991 (2025).
62. Perez-Garcia, L. & Amabilino, D. B. Spontaneous Resolution, Whence and Whither: From enantiomorphous solids to chiral liquid crystals, monolayers and macro- and supramolecular polymers and assemblies. *Chem. Soc. Rev.* **36**, 941–967 (2007).
63. Gong, W., Chen, Z., Dong, J., Liu, Y. & Cui, Y. Chiral metal–organic frameworks. *Chem. Rev.* **122**, 9078–9144 (2022).
64. Kim, J. H., Schembri, T., Bialas, D., Stolte, M. & Würthner, F. Slip-stacked j-aggregate materials for organic solar cells and photodetectors. *Adv. Mater.* **34**, 2104678 (2022).
65. Li, H. et al. Nucleation and growth of covalent organic frameworks from solution: the example of COF-5. *J. Am. Chem. Soc.* **139**, 16310–16318 (2017).
66. Wang, S. et al. Pathway complexity in the stacking of imine-linked macrocycles related to two-dimensional covalent organic frameworks. *Chem. Mater.* **31**, 7104–7111 (2019).
67. Achalkumar, A. S., Hiremath, U. S., Rao, D. S. S., Prasad, S. K. & Yelamaggad, C. V. Self-assembly of hekates-tris(n-salicylideneaniline)s into columnar structures: synthesis and characterization. *J. Org. Chem.* **78**, 527–544 (2013).
68. Wöhrle, T. et al. Discotic liquid crystals. *Chem. Rev.* **116**, 1139–1241 (2016).
69. Piechocka, I. K., Bacabac, R. G., Potters, M., MacKintosh, F. C. & Koenderink, G. H. Structural hierarchy governs fibrin gel mechanics. *Biophys. J.* **98**, 2281–2289 (2010).
70. Zhang, M. et al. Mandrel-free fabrication of giant spring-index and stroke muscles for diverse applications. *Science* **387**, 1101–1108 (2025).

Acknowledgements

This work was financially supported by the Strategic Priority Research Program of CAS (XDB0520201 to D.W.), CAS Project for Young Scientists in Basic Research (YSBR-053 to D.W.), the National Natural Science Foundation of China (22421001 to D.W., 22402205 to L.W., and 22132007 to D.W.), and the China Postdoctoral Science Foundation funded project (Grant No. 2024M763322 to L.W.). The authors gratefully thank Bo Guan, Jiling Yue, and Kaiang Liu for their assistance in low-dose HRTEM imaging. The authors gratefully thank Zhen Zhang, Chuang Zhang, Lang Jiang, Yunlong Guo, Jian Jiang, and Anna Painelli for valuable discussions.

Author contributions

X.-R.R. and B.K. designed and synthesized the materials and performed characterization experiments. X.-R.R., B.K., and D.W. interpreted the results and wrote the manuscript. Q.H., F.B., Y.X., L.W., Z.-L.Z., and T.C. assisted in data analysis. D.W. and L.-J.W. supervised the project. All authors discussed the results and contributed to the manuscript.

Competing interests

The authors declare no competing interests.

Additional information

Supplementary information The online version contains supplementary material available at <https://doi.org/10.1038/s41467-025-66586-y>.

Correspondence and requests for materials should be addressed to Dong Wang.

Peer review information *Nature Communications* thanks Wei-Guang Zhang and the other, anonymous, reviewer(s) for their contribution to the peer review of this work. A peer review file is available.

Reprints and permissions information is available at <http://www.nature.com/reprints>

Publisher's note Springer Nature remains neutral with regard to jurisdictional claims in published maps and institutional affiliations.

Open Access This article is licensed under a Creative Commons Attribution-NonCommercial-NoDerivatives 4.0 International License, which permits any non-commercial use, sharing, distribution and reproduction in any medium or format, as long as you give appropriate credit to the original author(s) and the source, provide a link to the Creative Commons licence, and indicate if you modified the licensed material. You do not have permission under this licence to share adapted material derived from this article or parts of it. The images or other third party material in this article are included in the article's Creative Commons licence, unless indicated otherwise in a credit line to the material. If material is not included in the article's Creative Commons licence and your intended use is not permitted by statutory regulation or exceeds the permitted use, you will need to obtain permission directly from the copyright holder. To view a copy of this licence, visit <http://creativecommons.org/licenses/by-nc-nd/4.0/>.

© The Author(s) 2025